Research Article Vol. 34, No. 8 / 20 Apr 2026 / *Optics Express* 15532

Optics EXPRESS

O-band 4×32 Gbit/s CWDM receiver on a silicon nitride photonic platform with micro-transfer printed InGaAs/InP photodiodes

SENBIAO QIN,[1,2,*] LAURENS BOGAERT,[1,2]
JASPER DE WITTE,[1,2] SANDER RENIERS,[3]
YUQING JIAO,[3] JING ZHANG,[1,2]
JOHAN BAUWELINCK,[4] AND GUNTHER ROELKENS[1,2]

[1] *Photonics Research Group, Ghent University-IMEC, 9052 Ghent, Belgium*
[2] *Center for Nano- and Biophotonics, Ghent University, Ghent, Belgium*
[3] *Eindhoven Hendrik Casimir Institute (EHCI), Eindhoven University of Technology, Eindhoven 5600MB, The Netherlands*
[4] *IDLab, Ghent University-IMEC, 9052 Ghent, Belgium*
[*] *senbiao.qin@ugent.be*

Abstract: We present an O-band four-channel coarse wavelength-division-multiplexed (CWDM) receiver implemented on a silicon nitride (SiN) photonic integrated circuit (PIC) platform, enabled by micro-transfer printing of InGaAs/InP photodiodes. The PIC incorporates a cascaded Mach–Zehnder interferometer (MZI) lattice filter demultiplexer and four high-speed photodiodes. The demultiplexer achieves low insertion loss (1.7–2.4 dB) and crosstalk below -14 dB across the 1270–1330 nm grid. The printed photodiodes exhibit responsivities of 0.54–0.72 A/W across the four channels and a 33 GHz 3-dB bandwidth at 1310 nm under a −2 V bias. High-speed back-to-back reception of 32 Gbit/s non-return-to-zero (NRZ) signals is demonstrated on all channels, yielding open eye diagrams and bit-error rates (BERs) below 10^{-4} at demultiplexer-received optical powers above −11 dBm, obtained without a transimpedance amplifier. These results underscore the potential of micro-transfer printed InGaAs/InP photodiodes on SiN as a scalable solution for high-speed O-band receivers in short-reach interconnects and optical I/O.

1. Introduction

The rapid advancement of artificial intelligence is driving a dramatic increase in bandwidth demand for data centers [1–4] and high-performance computing systems [4–7]. Silicon photonics (SiPh) provides a much higher bandwidth density than conventional copper interconnects, making it a key enabling technology for next-generation optical links. State-of-the-art SiPh platforms, such as imec’s iSiPP50G, provide essential building blocks–including high-speed modulators, Ge photodetectors, and WDM filters–through cost-effective and highly scalable manufacturing processes [8]. More recently, chiplet-based optical I/O architectures compatible with UCIe have been proposed to address the bandwidth, power, and reach limitations of electrical interconnects in AI scale-up systems by employing highly parallel optical lanes at moderate per-lane data rates (e.g., 32 Gbit/s) to achieve terabit-class aggregate bandwidth [9].

Compared with silicon (Si), SiN offers several distinct advantages, including a broad transparency window from 400 to 4000 nm, negligible two-photon absorption, and ultralow waveguide loss below 1 dB/m that has been experimentally demonstrated in prior work [10]. SiN also provides superior thermal stability: its thermo-optic coefficient is 2.45×10^{-5} /°C, approximately one-seventh that of silicon. Consequently, the thermal sensitivity of a typical silicon-on-insulator (SOI) CWDM filter is around 70–80 pm/°C [11], whereas for SiN it is only 14–19 pm/°C [11–13].

#590225
Journal © 2026

https://doi.org/10.1364/OE.590225
Received 13 Jan 2026; revised 26 Feb 2026; accepted 26 Feb 2026; published 16 Apr 2026

In Ref. [13], a SiN (de-)multiplexer designed for data and computing communications was demonstrated to operate reliably at temperatures up to 80 °C.

While SiN enables low-loss and thermally stable passive circuits, it lacks native photodetection capability. Heterogeneous integration of III–V photodiodes onto SiN therefore plays a critical role in realizing fully integrated receivers. Micro-transfer printing is an efficient and scalable approach for integrating high-performance active devices onto Si/SiN photonic platforms with high placement accuracy, high throughput, and excellent yield [14–18]. This technique is particularly suitable for integrating compact, high-bandwidth InGaAs/InP photodiodes at the output ports of complex wavelength-selective circuits.

Recent demonstrations have shown the feasibility of integrating III–V photodiodes on SiN using micro-transfer printing [19,20]. In this work, we present an O-band four-channel CWDM receiver PIC fabricated on a 300 nm low-pressure chemical vapor deposition (LPCVD) SiN platform and integrated with micro-transfer printed InGaAs/InP photodiodes. The device incorporates a compact cascaded MZI lattice filter demultiplexer with low insertion loss and low crosstalk, together with high-speed photodiodes exhibiting a 33 GHz 3-dB bandwidth. We demonstrate 32 Gbit/s NRZ reception across all four wavelength channels, achieving BER values below the HD-FEC threshold. To the best of our knowledge, this is one of the first demonstrations of a four-channel O-band CWDM receiver on SiN using micro-transfer printed photodiodes capable of >30 Gbit/s operation, paving the way for energy-efficient and scalable optical-interconnect solutions.

2. Design and fabrication

The fabricated O-band four-channel CWDM receiver PIC is shown in Fig. 1. The device is implemented on a 300 nm LPCVD SiN platform, featuring a 1.1-μm-wide SiN stripe waveguide and a 1.8 μm divinylsiloxane-bis-benzocyclobutene (DVS-BCB) cladding layer. The total footprint of the receiver is 3300 μm × 2200 μm. It comprises a demultiplexer and four micro-transfer printed InGaAs/InP photodiodes.

The demultiplexer employs a cascaded MZI lattice filter architecture that offers both a wide and flat passband as well as low insertion loss [21]. In this configuration, the first stage separates the odd and even channels, while the second stage further resolves the individual wavelengths. A schematic of the O-band four-channel demultiplexer is shown in Fig. 2. Each four-port lattice filter comprises two cascaded MZIs, incorporating three directional couplers and two delay lines. The power cross-coupling coefficients (κ) of the three directional couplers are 0.50, 0.29, and 0.08, as adopted from Ref. [21].

The lengths of the delay lines are determined by the target channel spacing of 20 nm. Accordingly, the free spectral ranges (FSRs) of the first and second stages are designed to be 40 nm and 80 nm, respectively. The FSR is inversely proportional to the delay length and is given by

$$FSR = \frac{\lambda^2}{n_g \Delta L}, \tag{1}$$

where λ is the center wavelength of interest and n_g is the group index of the waveguide at this wavelength. For the calculation, $n_g = 1.97$ at $\lambda = 1.305$ μm was adopted.

For each filter stage, the two delay lines are with lengths of ΔL and $2\Delta L$. Based on Eq. (1), the delay line length parameters for the first and second stages are calculated to be $\Delta L_1 = 21.60$ μm and $\Delta L_2 = 10.80$ μm, respectively.

In the lower arm of the second stage, the delay line length is slightly adjusted to introduce an additional $3\pi/2$ phase shift, enabling alignment of the passbands with the target wavelength grid. The required additional delay length is given by

$$\Delta L' = \frac{3\lambda}{4n_{\text{eff}}}, \tag{2}$$

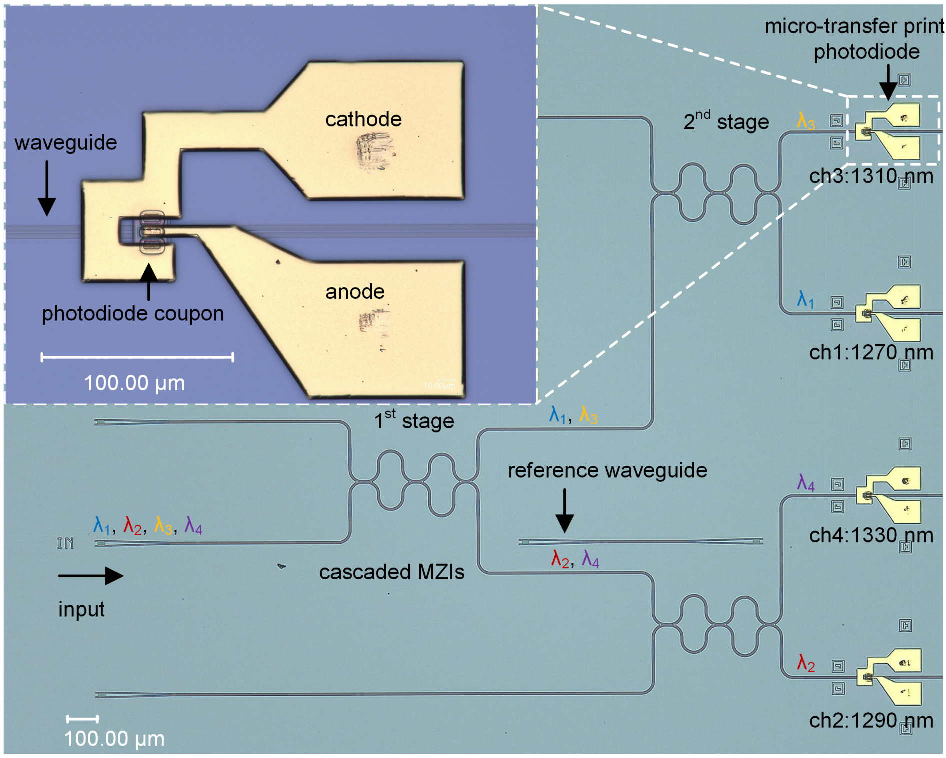

Fig. 1. Microscope image of the O-band four-channel CWDM receiver PIC, with the inset showing a magnified view of a micro-transfer printed photodiode.

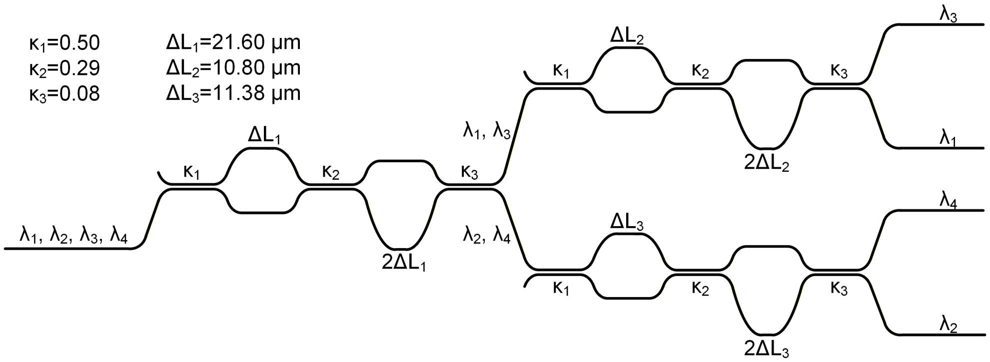

Fig. 2. Schematic of the O-band four-channel demultiplexer.

where n_{eff} (~1.67) is the effective index of the waveguide. As a result, the adjusted delay line length parameter is determined to be $\Delta L_3 = 11.38\ \mu\text{m}$.

Optical signals are coupled into the chip via a grating coupler. Its insertion loss is characterized using a reference waveguide located at the center of the PIC and subsequently deembedded. The photodiodes are integrated at the output ports through micro-transfer printing, enabling evanescent coupling of the optical signals from the SiN waveguides into the photodiodes. The inset in Fig. 1 provides a magnified view of a printed photodiode. Each photodiode coupon is placed on top of the waveguide and features cathode and anode metal pads for electrical probing.

The photodiode design, fabrication, and integration follow the methods reported in Ref. [19]. Figure 3(a)–(c) show microscope images of the photodiode coupons on the III–V source sample, a photodiode printed onto a SiN waveguide, and a micro-transfer printed device after final metallization, respectively. The overall integration flow is outlined in Fig. 3(d). Briefly, printable photodiode coupons were first fabricated on an III–V source wafer and subsequently transfer-printed onto a pre-patterned SiN PIC using a PDMS stamp. After printing, standard post-printing processes, including photoresist removal, DVS-BCB coating and curing, via opening, and final metallization, were carried out to complete the device integration.

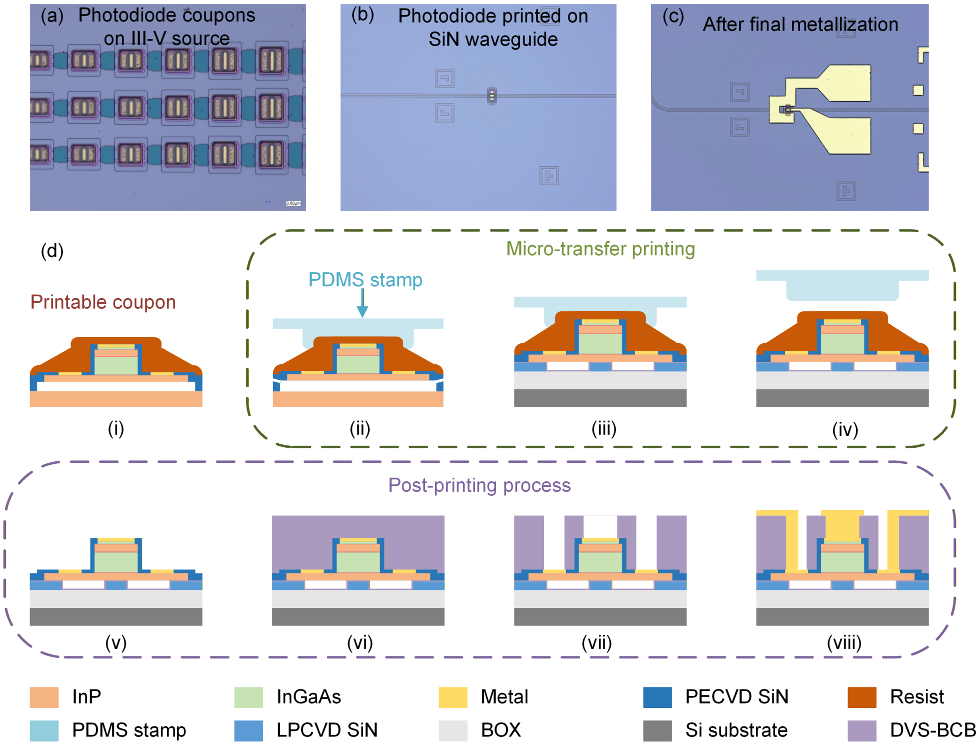

Fig. 3. Integration process of photodiodes using micro-transfer printing. (a) Microscope image of photodiode coupons on the III–V source sample. (b) Microscope image of a photodiode printed onto a SiN waveguide. (c) Microscope image of a micro-transfer printed photodiode after final metallization. (d) Schematic overview of the micro-transfer printing and post-printing processes.

3. Characterization and discussion

All measurements reported in this section were performed with the sample mounted on a thermoelectric cooler (TEC), with the temperature stabilized at 23 °C.

3.1. Performance of the O-band four-channel demultiplexer

The performance of the demultiplexer was characterized using a reference structure without printed photodiodes. The measured transmission spectra are shown in Fig. 4. The spectra were normalized to a reference waveguide on the same chip to remove the grating coupler losses (see Appendix A). The device exhibits an FSR of 77 nm, which is divided into four wavelength channels at 1270, 1290, 1310, and 1330 nm, respectively. The key performance metrics of the demultiplexer are summarized in Table 1. The measured insertion losses are 2.4 dB at 1270 nm, 2.0 dB at 1290 nm, 1.7 dB at 1310 nm, and 2.4 dB at 1330 nm, with corresponding crosstalk levels of −14.4, −17.4, −14.0, and −16.6 dB. The reported crosstalk values were extracted by comparing the transmission of each channel with the maximum leakage from the other channels at the same wavelength.

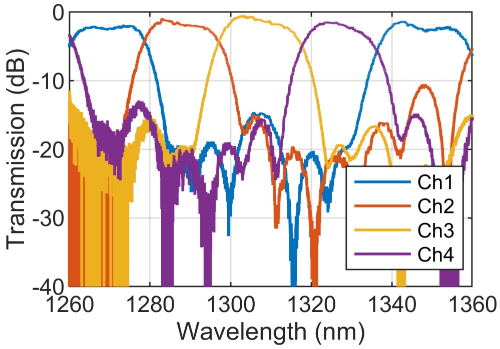

Fig. 4. Measured transmission spectra of a reference four-channel demultiplexer, normalized to a reference waveguide to remove the grating coupler losses.

Table 1. Metrics of the demultiplexer

Metrics	ch1: 1270 nm	ch2: 1290 nm	ch3: 1310 nm	ch4: 1330 nm
Insertion loss (dB)	2.4	2.0	1.7	2.4
Crosstalk (dB)	−14.4	−17.4	−14.0	−16.6

Expected thermal robustness of the SiN-based demultiplexer. As discussed in the Introduction, the SiN platform offers an intrinsically low thermo-optic coefficient compared to Si, which translates into improved wavelength stability of passive photonic circuits. In the demonstrated receiver, this platform-level advantage directly benefits the cascaded MZI lattice demultiplexer, whose wide passband relaxes sensitivity to small temperature-induced wavelength shifts.

While a systematic temperature-dependent characterization of the complete receiver is beyond the scope of this work, the combination of the SiN platform and the lattice filter architecture is expected to provide robust operation under moderate temperature variations. Future work will focus on experimentally quantifying the temperature tolerance of the integrated receiver.

Fabrication tolerance and phase error considerations. In cascaded MZI lattice filters, process variations, such as small deviations in waveguide width and effective index, can introduce phase errors in the interferometric delay arms. These phase errors may lead to passband misalignment with respect to the designed wavelength grid and result in wavelength-dependent performance variations, including differences in insertion loss and inter-channel crosstalk among the CWDM channels.

In the present work, the sensitivity to such phase errors is mitigated by employing relatively wide (1.1 μm) single-mode TE SiN stripe waveguides in the delay arms. Compared to SiPh platforms, the lower refractive-index contrast of the SiN/SiO_2/BCB system inherently reduces the sensitivity of the optical phase to fabrication-induced dimensional variations. As a result, phase errors in SiN-based interferometric circuits are expected to be smaller for a given level of process variation.

While the measured transmission spectra indicate that the remaining wavelength-dependent variations are limited, further reduction of phase errors would ultimately rely on improvements in fabrication accuracy rather than design-level modifications alone.

3.2. Performance of the micro-transfer printed photodiodes

The performance of the micro-transfer printed photodiodes was characterized using a reference device fabricated on the same PIC sample. Figure 5(a) shows a microscope image of the reference structure, which includes a grating coupler for optical input and metal pads for GSG probing. The measured I–V characteristics are presented in Fig. 5(b), showing a dark current of 100 nA at a bias voltage of −2 V.

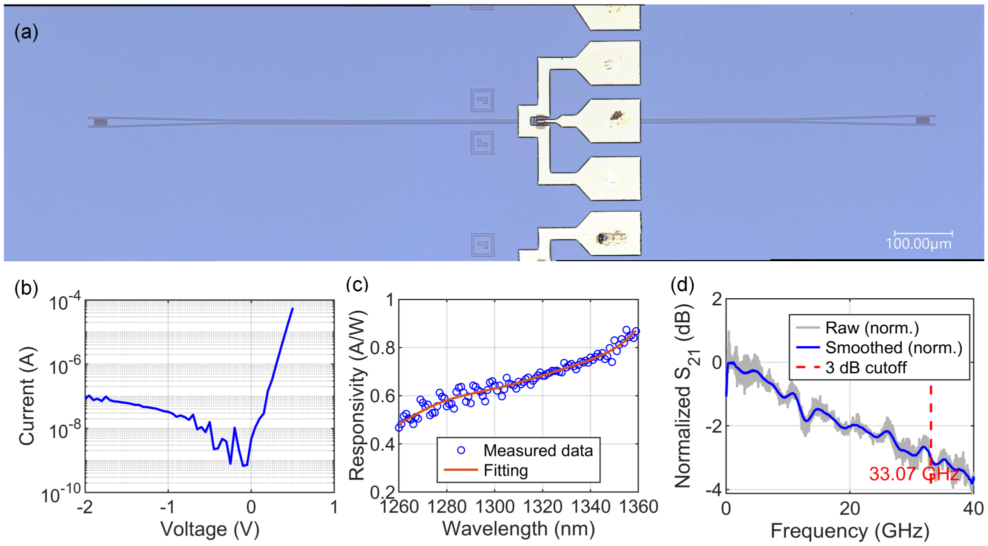

Fig. 5. Measured performance of the reference photodiode. (a) Microscope image of the device. (b) I–V characteristics. (c) Measured responsivity over the wavelength range of 1260–1360 nm, after removing the grating coupler loss. (d) S_{21} measurement at 1310 nm with the device biased at −2 V.

The responsivity referenced to the waveguide-coupled optical power over the wavelength range of 1260–1360 nm is plotted in Fig. 5(c), where the grating-coupler loss has been de-embedded (see Appendix A). At 1270, 1290, 1310, and 1330 nm, the measured responsivities are 0.54, 0.61, 0.65, and 0.72 A/W, respectively. The 3-dB bandwidth of the device at 1310 nm, biased at −2 V, is 33.07 GHz, extracted from the measured S_{21} response shown in Fig. 5(d).

Discussion on bandwidth limitations and device reproducibility. The measured 3-dB bandwidth is primarily limited by the RC time constant of the device rather than by carrier transit time [19]. In the present design, the junction capacitance is mainly determined by the photodiode geometry and depletion region thickness defined at the coupon fabrication stage, where the mesa dimension is 13 μm × 6 μm (corresponding to an active area of 78 μm^2).

As all photodiode coupons are fabricated using the same epitaxial structure and lithographic process on the III–V source wafer, similar junction capacitance and intrinsic RC-limited bandwidth are expected for all printed devices. Variations in optical coupling efficiency among printed photodiodes may arise from small placement offsets and local process variations during integration; however, such variations predominantly affect the measured responsivity and have a limited impact on the intrinsic electrical bandwidth.

The use of micro-transfer printing enables accurate placement of pre-fabricated photodiode coupons with high yield, supporting the scalability of this integration approach. A detailed device-to-device statistical analysis of the bandwidth is left for future work.

3.3. High-speed large-signal reception experiment

The high-speed reception performance of the receiver was evaluated using back-to-back eye diagram measurements, using the measurement setup as shown in Fig. 6. A 32 Gbit/s NRZ data stream based on a pseudo-random binary sequence (PRBS) of length $2^7 - 1$ was generated at 1270, 1290, 1310, and 1330 nm using an O-band tunable laser, a 40 Gbit/s MZM, and an arbitrary waveform generator (AWG, Keysight M9502A). The RF signal from AWG was amplified to drive the MZM. The response of the external cables and connectors was pre-compensated using the AWG software. The modulated optical signal was subsequently amplified by an O-band praseodymium-doped fiber amplifier (PDFA), followed by a tunable optical filter to suppress amplified spontaneous emission (ASE) noise. A variable optical attenuator was employed to control the input optical power. The signal was then coupled into the PIC through the input grating coupler and sequentially detected at the output ports by the integrated photodiodes, which were biased at −2 V. The generated RF signals were amplified by an SHF S807 RF amplifier and then recorded on a sampling oscilloscope (Agilent DCA-X 86100D). The eye diagrams were captured directly from the oscilloscope display.

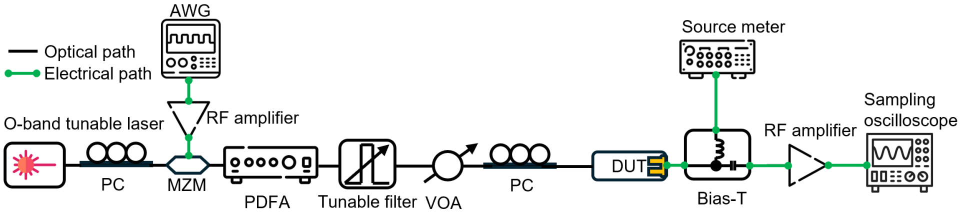

Fig. 6. Back-to-back eye diagram measurement setup.

The resulting back-to-back eye diagrams are shown in Fig. 7. During the measurement, the optical power was referenced to the waveguide power in front of the demultiplexer. All four channels operated at 32 Gbit/s NRZ with a demultiplexer-received optical power of −4.5 dBm and a photodiode bias of −2 V. The measured eye diagram SNRs for 1270, 1290, 1310, and 1330 nm were 6.43, 5.78, 5.83, and 5.86, respectively.

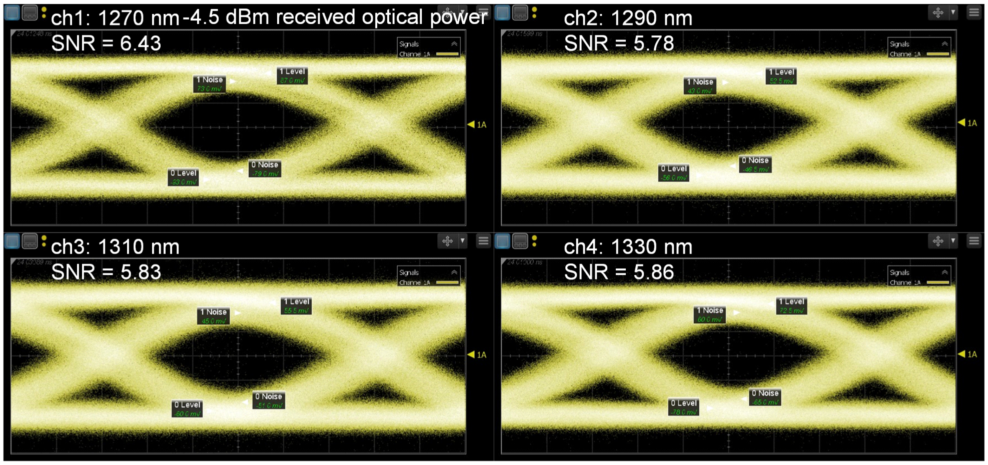

Fig. 7. Back-to-back measured eye diagrams for the 4 channels operating with 32 Gbit/s NRZ signals at a demultiplexer-received optical power of −4.5 dBm, with the photodiodes biased at −2 V.

In addition, the BER was measured as a function of the demultiplexer-received optical power for all four channels, as shown in Fig. 8. When the demultiplexer-received optical power exceeded −11 dBm, the BER values for all channels remained below 10^{-4}. The BER was derived from the SNR of the measured eye diagrams according to the Gaussian BER estimation (see Appendix B). At lower demultiplexer-received optical powers, the eye diagrams became too noisy to allow accurate SNR extraction, thereby preventing reliable BER estimation.

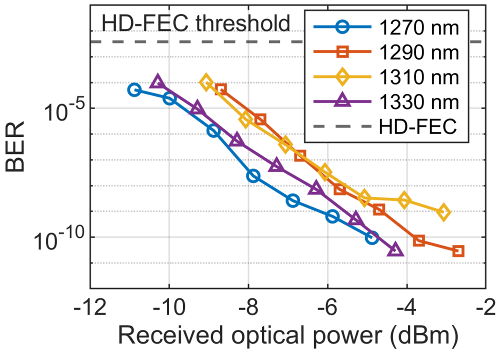

Fig. 8. Back-to-back BER performance of the four channels as a function of demultiplexer-received optical power for 32 Gbit/s NRZ operation, with the photodiodes biased at −2 V.

Analysis of channel-to-channel sensitivity variation. It can also be observed that the 1270 nm and 1330 nm channels exhibit better sensitivity compared with the 1290 nm and 1310 nm channels. The observed sensitivity variation among the channels can be attributed to a combination of factors, including the wavelength-dependent responsivity of the photodiodes, uncertainties in the insertion loss of the individual demultiplexer channels, and calibration inaccuracies of the grating coupler loss across different wavelengths.

The observed sensitivity differences among the four channels can be quantified to first order by the effective optical-to-electrical conversion gain of each channel, which scales with the product of the demultiplexer transmission and the photodiode responsivity. With the optical power referenced to the waveguide in front of the demultiplexer, the detected electrical signal amplitude is proportional to

$$G_i \propto R_i \times 10^{-IL_i/10}, \tag{3}$$

where R_i is the responsivity and IL_i is the demultiplexer insertion loss of channel i.

Using the measured values ($IL = 2.4/2.0/1.7/2.4$ dB and $R = 0.54/0.61/0.65/0.72$ A/W for 1270/1290/1310/1330 nm, respectively), the relative gains G_i (normalized to the best-performing channel) are approximately 0.71/0.88/1.00/0.94, corresponding to −1.51/−0.58/0/−0.26 dB. This indicates that the channel-to-channel sensitivity variation is largely explained by the combined effect of responsivity and demultiplexer insertion loss.

In addition, wavelength-dependent uncertainties in the grating-coupler calibration can introduce further apparent channel-to-channel variations and are likely responsible for the remaining mismatch between the simple gain-based estimate and the experimentally extracted BER trends. In practical systems, such variations can be readily mitigated by per-channel optical power leveling and/or electrical equalization, and therefore do not necessarily require a redesign of the demultiplexer.

Expected impact of inter-channel crosstalk in multi-wavelength operation. In the back-to-back large-signal experiments, the eye diagrams were recorded by launching and detecting one wavelength channel at a time. Therefore, the measured eye diagrams and the corresponding SNR-derived BER mainly reflect the receiver performance in the absence of simultaneous data modulation on the other CWDM channels.

In a practical multi-wavelength operation scenario, inter-channel crosstalk from the demultiplexer would appear as an additional interfering signal at the photodiode input. Based on the measured demultiplexer crosstalk levels (≤ –14 dB), the worst-case leaked optical power from an adjacent channel is ≤ 4% of the desired channel power. For uncorrelated data streams, such leakage primarily manifests as an additional noise-like impairment and is expected to cause limited eye closure and sensitivity penalty.

In addition to optical crosstalk, multi-channel receivers may also be affected by electrical crosstalk arising from closely spaced electrodes and RF interconnects. In future iterations, utilizing a GSG electrode configuration is expected to further reduce channel-to-channel electrical crosstalk by confining the electromagnetic fields and minimizing capacitive and inductive coupling between adjacent signal lines.

3.4. *Comparison with prior CWDM and WDM receivers*

To contextualize the demonstrated receiver at the system level, Table 2 provides a concise comparison with representative SiN-based CWDM devices and Si-based WDM receivers reported in the literature. As summarized in the table, SiN platforms have predominantly been explored for passive CWDM wavelength-selective components, whereas receiver-level implementations are more commonly realized on Si using monolithically integrated Ge photodiodes or Ge/Si avalanche photodiodes (APDs) in combination with electronic front-ends.

Table 2. Concise system-level comparison with representative SiN-based CWDM devices and silicon-based WDM receivers

Work	PD integration	Electronics	Data rate / BW	Scope / Remarks
This work	μTP InGaAs/InP	None	4×32 Gbit/s 33 GHz	PIC-level CWDM receiver on SiN
Reference [13]	–	–	–	Passive CWDM demultiplexer
Reference [22]	–	–	–	Passive CWDM scalability study
Reference [23]	Ge	WB TIA	4×50 Gbit/s 50 GHz	Si-based WDM receiver
Reference [24]	Ge/Si APD	External	25 Gbit/s 25 GHz	Si-based DWDM receiver

The present work bridges this gap by demonstrating a fully integrated O-band CWDM receiver on a SiN platform enabled by micro-transfer printing of high-speed InGaAs/InP photodiodes, achieving four-channel 32 Gbit/s reception without the use of transimpedance amplifiers. Owing to the low thermo-optic coefficient of SiN, the use of a SiN platform is expected to reduce sensitivity to temperature variations compared to Si-based implementations, potentially alleviating the reliance on active thermal tuning.

In the present implementation, the overall footprint of the receiver is primarily determined by the waveguide routing rather than by the MZI lattice filters themselves, and could be further reduced through layout optimization. Compared to other heterogeneous integration approaches such as hybrid bonding or flip-chip photodiode integration, micro-transfer printing offers improved scalability and flexibility for integrating multiple photodiodes on passive SiN photonic circuits, while maintaining a compact and system-level integrated receiver architecture.

4. Conclusion

We have demonstrated a four-channel O-band CWDM receiver on a SiN photonic platform with integrated high-speed InGaAs/InP photodiodes enabled by micro-transfer printing. The cascaded MZI lattice filter demultiplexer provides low insertion loss and low crosstalk across the CWDM wavelength grid. The integrated photodiodes exhibit responsivities up to 0.72 A/W and a 33 GHz bandwidth, enabling 32 Gbit/s NRZ detection across all channels. Back-to-back measurements confirm open eye diagrams and BER levels below 10^{-4} at demultiplexer-received optical powers above –11 dBm. These results validate the suitability of micro-transfer printed photodiodes for high-speed SiN-based receivers and highlight the potential of this heterogeneous integration approach for future multi-wavelength short-reach optical interconnects.

Appendix A. Grating coupler transmission characterization

The transmission spectrum of the input grating coupler was characterized using a reference waveguide located on the same chip. The measured transmission over the wavelength range of 1260–1360 nm is shown in Fig. 9.

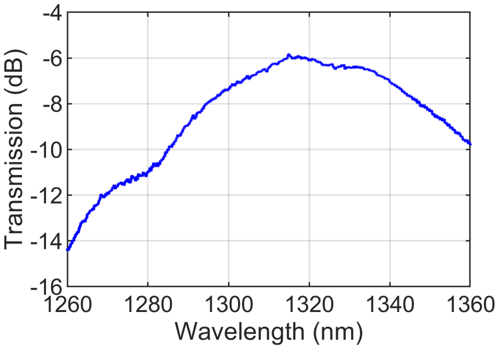

Fig. 9. Measured transmission spectrum of the grating coupler, characterized using a reference waveguide on the same chip.

The grating coupler exhibits a peak transmission of approximately −6 dB around 1315–1320 nm. At the CWDM channel wavelengths (1270, 1290, 1310, and 1330 nm), the measured transmission values are approximately −11.9 dB, −8.9 dB, −6.5 dB, and −6.4 dB, respectively.

All reported device metrics in the main text, including responsivity and demultiplexer insertion loss, are normalized to the waveguide power by de-embedding the grating coupler loss using this reference measurement.

Appendix B. Gaussian BER estimation based on eye diagram SNR

In this work, the BER is estimated from the measured eye diagram SNR. The eye diagram SNR is defined as

$$\mathrm{SNR} = \frac{\mu_1 - \mu_0}{\sigma_1 - \sigma_0}, \tag{4}$$

where μ_1 and μ_0 denote the mean voltage levels of the logical “1” and “0”, respectively, and σ_1 and σ_0 are the corresponding standard deviations extracted from the eye diagram.

Under the assumption of additive white Gaussian noise and symmetric decision thresholds, the BER for NRZ signaling can be approximated as

$$\mathrm{BER} \approx \frac{1}{2}\mathrm{erfc}\left(\frac{\mathrm{SNR}}{\sqrt{2}}\right). \tag{5}$$

The measured eye diagrams shown in Fig. 7 exhibit clear eye openings without pronounced pattern-dependent distortions, indicating that the system is primarily noise-limited rather than inter-symbol-interference (ISI)-limited. Under such conditions, the noise distributions associated with logical “0” and “1” can be reasonably approximated as Gaussian. Nevertheless, it is acknowledged that Gaussian BER estimation may underestimate the true BER in the presence of residual ISI or other non-Gaussian noise contributions, particularly when extrapolated to very low BER levels (e.g., below 10^{-12}). In the present work, the estimated BER remains above this regime, where Gaussian-based BER estimation is generally considered to provide a reasonable approximation of system performance.

Funding. UGent BOF-GOA project Optical Network-on-Wafer; Fonds Wetenschappelijk Onderzoek (FWO) (1S69123N).

Acknowledgment. S.Q. acknowledges Joris Van Kerrebrouck, Nishant Singh, Clemens Krückel, and Yujie Guo for their support with measurements, as well as Steven Verstuyft, Muhammad Muneeb, Elif Özçeri İyikanat, Peter Geerinck and Liesbet Van Landschoot for their assistance with fabrication.

Disclosures. The authors declare no conflicts of interest.

Data availability. Data underlying the results presented in this paper are not publicly available at this time but may be obtained from the authors upon reasonable request.

References

1. R. G. Beausoleil, M. McLaren, and N. P. Jouppi, "Photonic architectures for high-performance data centers," IEEE J. Sel. Top. Quantum Electron. **19**(2), 3700109 (2013).
2. R. Blum, "Integrated silicon photonics for high-volume data center applications," Optical Interconnects XX **11286**, 19–149 (2020).
3. Z. Zhou, R. Chen, X. Li, *et al.*, "Development trends in silicon photonics for data centers," Opt. Fiber Technol. **44**, 13–23 (2018).
4. S. B. Yoo, "Prospects and challenges of photonic switching in data centers and computing systems," J. Lightwave Technol. **40**(8), 2214–2243 (2022).
5. M. A. Taubenblatt, "Optical interconnects for high performance computing," in *IEEE Photonic Society 24th Annual Meeting*, (2011), pp. 668–669.
6. S. Zhang, Z. Zhang, M. Naderan-Tahan, *et al.*, "Photonic network-on-wafer for multichiplet gpus," IEEE Micro **43**(2), 86–95 (2023).
7. P. Ossieur, B. Moeneclaey, G. Coudyzer, *et al.*, "Integrated photonics and electronics for optical transceivers supporting ai/ml applications," IEEE J. Sel. Top. Quantum Electron. **31**(3: AI/ML Integrated Opto), 1–16 (2025).
8. F. Ferraro, P. De Heyn, M. Kim, *et al.*, "Imec silicon photonics platforms: performance overview and roadmap," in *Next-Generation Optical Communication: Components, Sub-Systems, and Systems XII*, vol. 12429 (SPIE, 2023), pp. 22–28.
9. P. Bhargava, S. Buchbinder, Đ. Gluhović, *et al.*, "A ucie optical i/o retimer chiplet for ai scale-up fabrics," in *Optical Fiber Communication Conference*, (Optica Publishing Group, 2025), pp. Th4B–3.
10. C. Xiang, W. Jin, and J. E. Bowers, "Silicon nitride passive and active photonic integrated circuits: trends and prospects," Photonics Res. **10**(6), A82–A96 (2022).
11. D. Tu, X. Huang, H. Yu, *et al.*, "400 gbps pam4 and 280 gbps nrz silicon photonic transmissions with fabrication-tolerant silicon nitride cwdm4 filters," J. Lightwave Technol. **42**(1), 302–308 (2024).
12. G. Gao, D. Chen, S. Tao, *et al.*, "Silicon nitride o-band (de)multiplexers with low thermal sensitivity," Opt. Express **25**(11), 12260–12267 (2017).
13. S. S. Cheung and M. R. T. Tan, "Silicon nitride (si3n4) (de-)multiplexers for 1-μm cwdm optical interconnects," J. Lightwave Technol. **38**(13), 3404–3413 (2020).
14. G. Roelkens, J. Zhang, L. Bogaert, *et al.*, "Micro-transfer printing for heterogeneous si photonic integrated circuits," IEEE J. Sel. Top. Quantum Electron. **29**(3: Photon. Elec. Co-Inte. and Ad), 1–14 (2023).
15. H. Deng, J. Zhang, E. Soltanian, *et al.*, "Single-chip silicon photonic engine for analog optical and microwave signals processing," Nat. Commun. **16**(1), 5087 (2025).
16. Y. Liu, Y. Chen, L. Bogaert, *et al.*, "Widely tunable narrow-linewidth lasers with booster amplification on silicon photonics," Opt. Express **33**(10), 22078–22086 (2025).
17. M. Niels, T. Vanackere, T. Vandekerckhove, *et al.*, "Centimetre-scale micro-transfer printing to enable heterogeneous integration of thin film lithium niobate with silicon photonics," Opt. Mater. Express **15**(3), 531–540 (2025).
18. M. Niels, E. Vissers, T. Vanackere, *et al.*, "Demonstration of lithium niobate integration on a 200-mm silicon photonics wafer using transfer printing," Opt. Lett. **50**(15), 4678–4681 (2025).
19. S. Qin, L. Bogaert, S. Reniers, *et al.*, "Micro-transfer printing of o-band ingaas/inp photodiodes on a silicon nitride photonic platform," Opt. Express **33**(16), 34153–34169 (2025).
20. D. Maes, S. Lemey, G. Roelkens, *et al.*, "High-speed uni-traveling-carrier photodiodes on silicon nitride," APL Photonics **8**(1), 016104 (2023).
21. F. Horst, W. M. Green, S. Assefa, *et al.*, "Cascaded mach-zehnder wavelength filters in silicon photonics for low loss and flat pass-band wdm (de-)multiplexing," Opt. Express **21**(10), 11652–11658 (2013).
22. A. Caut, M. Girardi, V. Torres-Company, *et al.*, "Channel scalability of silicon nitride (de-) multiplexers for optical interconnects at 1 m," J. Lightwave Technol. **42**(1), 276–286 (2024).
23. M. Moralis-Pegios, S. Pitris, T. Alexoudi, *et al.*, "4-channel 200 gb/s wdm o-band silicon photonic transceiver sub-assembly," Opt. Express **28**(4), 5706–5714 (2020).
24. D. Liang, S. Srinivasan, G. Kurczveil, *et al.*, "An energy-efficient and bandwidth-scalable dwdm heterogeneous silicon photonics integration platform," IEEE J. Sel. Top. Quantum Electron. **28**(6), 1–19 (2022).